ACS NANO

www.acsnano.org

ARTICLE

The Surface of Colloidal Metal–Organic Framework Nanoparticles Revealed by Vibrational Sum Frequency Scattering Spectroscopy

Ashley N. Mapile, Michael A. LeRoy, Kevin Fabrizio, Lawrence F. Scatena, and Carl K. Brozek*

Cite This: *ACS Nano* 2024, 18, 13406–13414

Read Online

ACCESS | Metrics & More | Article Recommendations | Supporting Information

ABSTRACT: **Solvation shells strongly influence the interfacial chemistry of colloidal systems, from the activity of proteins to the colloidal stability and catalysis of nanoparticles. Despite their fundamental and practical importance, solvation shells have remained largely undetected by spectroscopy. Furthermore, their ability to assemble at complex but realistic interfaces with heterogeneous and rough surfaces remains an open question. Here, we apply vibrational sum frequency scattering spectroscopy (VSFSS), an interface-specific technique, to colloidal nanocrystals with porous metal–organic frameworks (MOFs) as a case study. Due to the porous nature of the solvent-particle boundary, MOF particles challenge conventional models of colloidal and interfacial chemistry. Their multiweek colloidal stability in the absence of conventional surface ligands suggests that stability may arise in part from solvation forces. Spectra of colloidally stable Zn(2-methylimidazolate)$_2$ (ZIF-8) in polar solvents indicate the presence of ordered solvation shells, solvent–metal binding, and spontaneous ordering of organic bridging linkers within the MOF. These findings help explain the unexpected colloidal stability of MOF colloids, while providing a roadmap for applying VSFSS to wide-ranging colloidal nanocrystals in general.**

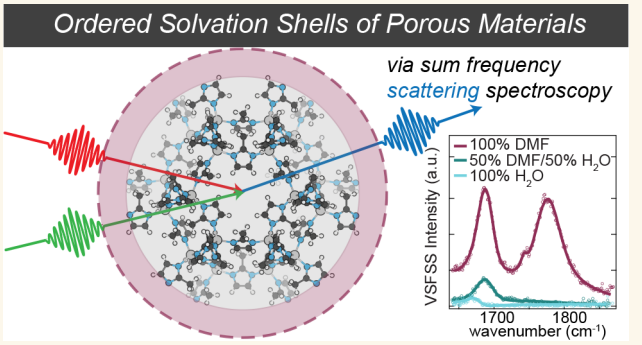

KEYWORDS: *sum frequency generation, metal–organic framework, nanocrystal, interface, solvation shell*

Solvation shells dictate the interactions between colloidal materials and their surroundings. The activity of proteins, for instance, derives from the structure and dynamics of hydration shells often nanometers thick and with behavior distinct from bulk water.[1,2] The properties of nanoparticles, from catalysis and particle growth mechanisms to plasmonics and colloidal stability, also depend on how solvent molecules structure around a particle surface.[3−5] Classically, according to continuum solvation models and Derjaguin–Landau–Verwey–Overbeek (DLVO) theory, colloidal stability depends only on electrostatic repulsion overcoming van der Waals attraction between particle surfaces.[6] When attractive interactions outweigh repulsion, as with metal nanoparticles and quantum dots, capping ligands provide additional steric and entropic repulsion.[7] Colloids without capping ligands and weak electrostatic forces are postulated to be stabilized by solvation shells that act as protective coatings.[8−10]

Available analytical tools reveal important but more general information about solvation shell structure and ordering. Atomic force measurement techniques, pioneered by Israelachvili et al., detect the presence of multilayer hydration shells on mica surfaces through oscillations in the steric friction upon approaching the particle surface.[11,12] Pair distribution function analysis of X-ray scattering data similarly suggests water self-assembles into ordered nanometer-thick layers at the surface of metal oxide nanoparticles, even when surfactant ligands are added to cap the particle surface.[3] Recently, second harmonic generation scattering experiments reveal pH- and salt-dependent ordering of water at the interface of colloidal SiO_2 and TiO_2 nanoparticles.[13,14] While these studies lay foundational

Received: March 20, 2024
Revised: April 10, 2024
Accepted: April 24, 2024
Published: May 9, 2024

evidence for ordered solvation shells, they lack the specificity necessary to identify both the chemical nature *and* the molecular conformation of solvation shells near metal nanoparticles. Such insights will be critical in understanding the chemistry of solvation shells assembled at complex interfaces. In particular, porous colloids pose considerable challenges and opportunities for studying interfacial phenomena due to their low surface-charge densities, the presence of both internal and external surfaces, and because void spaces comprise a significant portion of the nanoparticle−solvent electrical double layer. Preliminary investigations of porous colloids include calculations that reveal significant fluctuations in the electrostatic potential of bare, mesoporous silica nanoparticles that are highly dependent on pore size.[15−19] Related studies have shown that the morphology of porous particles influences the ordering of solvation shells and overall colloidal stability.[20] To understand how factors such as pore topology, molecular composition, and particle size influence the colloidal stability of porous materials, spectroscopic techniques are needed to uncover the arrangement of molecules at solvated nanoparticle surfaces.

Developed by Roke et al.,[21] vibrational sum frequency scattering spectroscopy (VSFSS) is a scattering adaptation of the reflection-based vibrational sum frequency spectroscopy introduced by Shen et al.[22] While reflection VSFS has been commonly used to probe planar air/water,[23] oil/water,[24] oxide/water,[25] and silica/water[26] interfaces, the scattering variation of this technique enables investigation into the interface of nanosized colloids.[27,28] VSFSS directly probes vibrational modes at interfaces due to selection rules prohibiting contributions from a centrosymmetric environment, such as a bulk liquid phase (Figure 1a). The signal indicates two main attributes of the chemical environment: the population of molecules at the interface and the average molecular orientation of vibrational modes, also referred to as net molecular ordering. Only highly ordered resonant vibrations generate a sum frequency response (Figure 1b). An overview of sum frequency scattering theory and its applications can be found in the Supporting Information and in other sources (Figure S4).[29,30] Another useful aspect of VSFSS is the ability to change the polarization of the incoming and collected beams to isolate vibrational responses from unique molecular orientations relative to the interface. A three-letter nomenclature denotes the polarization of the beams in the sum frequency, visible, and IR beams (Figure 1c). In this work, we use *ssp*, *sps*, and *ppp* polarization schemes. The *ssp* polarization scheme probes IR transition moments perpendicular to the interface, while the *sps* polarization probes IR transition moments aligned parallel to the interface. The *ppp* polarization combination probes a combination of transition moments in both the perpendicular and parallel contributions.

While VSFSS has been used extensively to study surfactant-stabilized nanoemulsions and ligand-capped particles, here we use VSFSS to probe a freestanding nanoparticle−solvent interface. Not only does our work assign discrete vibrational modes to solvent molecules and their relative orientation to the interface, but we also provide insight into the interfacial structure of both traditional metal oxide nanoparticles and the largely uninvestigated porous metal−organic framework nanoparticles whose surface is significantly less dense than their metal oxide counterparts.

Colloidal nanocrystals of porous solids stand in stark contrast with the "hard-shell" colloids well-suited to conventional models of interfacial chemistry. Metal−organic frameworks (MOFs), in particular, possess the highest accessible surface areas of any known material.[31] Unlike conventional nanoparticles, void spaces of nanometer-sized pores dominate the external surfaces of MOF nanoparticles (nanoMOFs). This scarcity of nanoparticle material at the interface should consequently lower the electrostatic repulsion and van der Waals attraction that dictate colloidal stability according to the DLVO theory. Such low-density architectures also create complex surfaces for the self-assembly of solvation shells due to their heterogeneous compositions and the presence of both internal and external surfaces accessible to the solvent. In the few existing synthetic methods for nanoMOFs, "modulators," rather than the typical surfactant ligands found in the quantum dot literature, direct the size of the nanoMOFs. Unlike surfactant ligands, evidence suggests modulators rarely incorporate onto exterior or interior surfaces. Instead, as described by the "seesaw" model, we reported recently, modulators influence particle sizes by affecting the metal-linker binding and linker deprotonation equilibria.[32,33] With this predictive model, we demonstrated a nanoparticle synthesis of the conductive MOF Fe(1,2,3-triazolate)$_2$ with diameter sizes controllable to just 6 nm—the smallest nanoMOFs to-date.[34] Size-dependent optical and charge-transport behavior emerged from this class of semiconductor nanocrystals distinct from those of traditional quantum dots. Despite the lack of surfactant additives and the absence of incorporated modulator, the particles exhibited indefinite colloidal stability in *N*,*N*-dimethylformamide (DMF) under anaerobic conditions. These observations suggest a mechanism of colloidal stability involving solvation shells, despite the

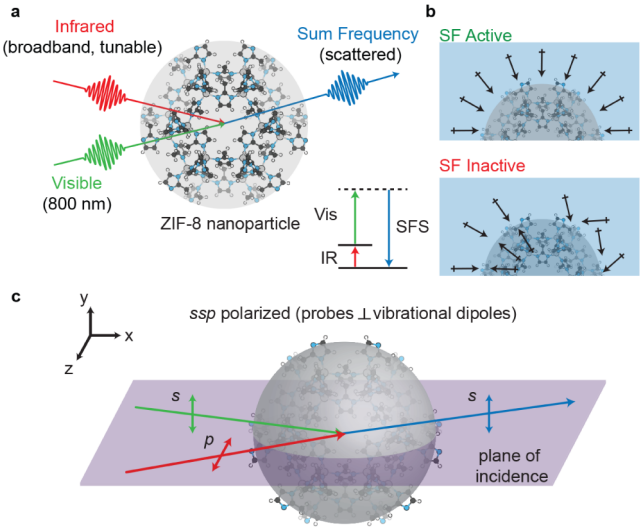

Figure 1. (a) Schematic of VSFSS, in which a sum frequency scattered response (blue) is generated by overlapping a visible (green) and IR (red) pulse spatially and temporally at the curved nanoMOF/solvent interface. The energy level diagram of the VSFSS is shown at the bottom right. (b) Cartoon representation of the possible scenarios in which a sum frequency signal could be expected. IR transition dipoles at anisotropic surfaces (top) are sum frequency active, while mismatched or directly opposing transition dipoles (bottom) are sum frequency inactive. (c) Schematic of the *ssp* polarization scheme in which the sum frequency, visible beams, and IR beams are *s*, *s*, and *p* polarized, respectively. This polarization combination probes vibrational dipoles perpendicular to an interface.

https://doi.org/10.1021/acsnano.4c03758
ACS Nano 2024, 18, 13406−13414

minimal amount of material at the particle surfaces, where the solvent could potentially bind. Nanoparticles of the commonly studied Zn-based MOF, ZIF-8 ($Zn(2\text{-methylimidazolate})_2$), also demonstrated long-term colloidal and air stability[35] (unlike $Fe(TA)_2$) in DMF, making them ideal candidates to study solvation shell chemistry. While ZIF-8 and other MOF species are known to be colloidally stable[36] and are frequently used in drug delivery platforms due to this attribute,[37] most cases require postsynthetic modification in the form of capping ligands, surfactants, or polymers to provide long-term stability and efficacy.[38−40] The mechanism of colloidal stability for bare nanoparticles, especially those with a low surface density, such as MOF nanoparticles, remains unknown. In applications, the ability to functionalize these nanoMOFs into polymer matrices to meet industrial demands for chemical separations and carbon capture will depend on surface interactions that contribute to this surfactant-free colloidal stability.[41,42] While others have studied the ligands of surface-coated nanoparticles[21,43,44] or bulk-sized MOF materials[45] through sum frequency techniques, herein, we investigate the solvent−particle interface of bare colloidal nanoparticles with long-term colloidal stability via VSFSS. Our results demonstrating the necessity of an ordered solvation shell for MOF colloidal stability are important for the varied uses of bare MOF nanoparticles, where the addition of a surface agent could have unintended consequences on optical properties, solution processability, solubility, and self-assembly.

RESULTS AND DISCUSSION

Ordered Solvation Shells Revealed by VSFSS. A colloidal suspension of nanoZIF-8 in DMF (SEM particle size of 316 nm and hydrodynamic diameter of 357 nm) was studied by VSFSS in the carbonyl stretching region of DMF (1600−1900 cm^{-1}) in three different polarization combinations (Figure 2a). As a control, VSFS spectra of bulk DMF were collected in all polarization combinations (Figure S5a−c), indicating that solvent absorption does not impact the spectral line-shapes reported here (Figure S5d). To test whether particle aggregates impact the observed sum frequency response, we pursued concentration-dependent size and polydispersity analysis as summarized in Figure S6. The *ssp* trace, which probes vibrational modes perpendicular to the interface, reveals two prominent features at 1689 and 1774 cm^{-1}. The significant signal intensity in this region indicates a large population of DMF molecules at the nanoMOF interface and indicates a high degree of ordering, as compared to previous VSFSS experiments that report relatively low signal intensity in the C═O region.[46,47] The presence of two distinct features indicates two significantly different chemical environments of the DMF C═O mode, which corroborates previous reports purporting the existence of multiple solvation shells at conventional nanoparticle surfaces.[3] Because both features are blue-shifted relative to DMF in bulk solution, these spectra indicate that the C═O bond of interfacial DMF strengthens upon association with the nanoparticle surface, as is consistent with coordination of DMF to Lewis acidic metal sites in the absence of π-back-bonding. To better understand the relative orientation of these vibrational modes, *ppp* and *sps* polarization combinations were employed. In *ppp*, the lower-frequency peak at 1689 cm^{-1} appears in higher intensity as compared to *ssp*, while the higher-frequency peak broadens and becomes less defined. On the other hand, in the *sps* polarization combination, the lower frequency peak disappears, while the higher frequency feature remains well-defined. Since we observe only the 1689 cm^{-1} feature under *ssp* polarization conditions, the C═O IR transition moment must be perpendicular to the nanoMOF surface (Figure 2a). We therefore assign the 1689 cm^{-1} feature to an ordered solvation shell of DMF molecules not directly bound to the surface Zn^{2+} sites (Figure 2c). A perpendicular arrangement of the DMF dipole to the particle surface would prevent the oxygen lone pairs on DMF from binding to surface Zn^{2+} sites. The increase in intensity of the 1689 cm^{-1} feature from *ssp* to *ppp* polarization can be attributed to an increase in specific tensor elements of $X^{(2)}$ (from 1 to 4) probed in the experiment.[30] As observed in other interfacial systems, most commonly with any hydrophobic/water interface, the presence of charge at an interface induces restructuring of solvent molecules into a net orientation.[3,14,48] Indeed, the positive zeta potential of ∼28 mV measured for these particles further supports the presence

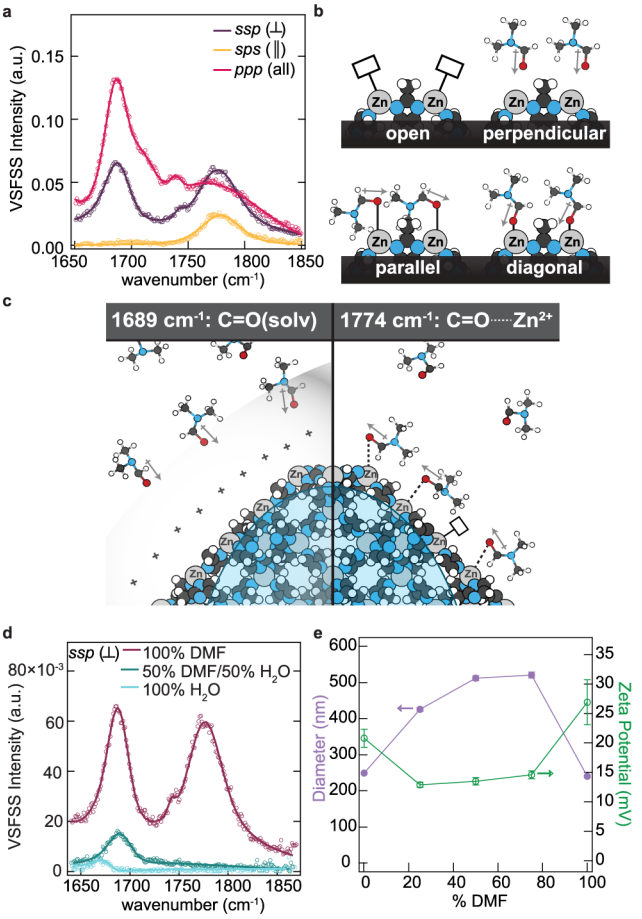

Figure 2. (a) VSFSS measurements of nanoZIF-8 particles suspended in DMF taken in the C═O stretching region in various polarization combinations. Lettering corresponds to the polarizations of the sum frequency, visible, and IR pulses. (b) Illustration of open metal sites on nanoZIF-8 and the orientation of carbonyl transition dipoles of DMF relative to the nanoMOF surface. (c) Illustration of different solvent ordering environments (solvation shell and metal binding) at the nanoZIF-8 interface. (d) VSFSS measurements (ssp polarization) of nanoZIF-8 particles dispersed in 100% DMF, 100% water, and a 50:50 mixture. In all VSFS spectra, open dots are raw data, while lines represent fits. (e) Hydrodynamic diameter (purple, closed dots) and surface zeta potential (green, open dots) measurements of nanoZIF-8 colloids suspended in varying ratios of water and DMF.

https://doi.org/10.1021/acsnano.4c03758
ACS Nano 2024, 18, 13406−13414

of a large surface charge and the presence of open metal sites.[49] We propose that this surface charge creates an electric field that aligns the dipoles of the DMF molecules in a perpendicular orientation. Previous studies have shown that colloidal mesoporous SiO_2 nanoparticles possess similar zeta potentials to ZIF-8 nanoparticles but display significantly reduced populations of ordered interfacial solvent as compared to their solid-interface counterparts.[15,20] The highly ordered solvation shells around nanoMOFs, on the other hand, may arise from the presence of open metal sites at uncapped MOF surfaces.[49−51] In spite of low surface densities, the zeta potentials of MOF particles with high concentrations of missing linker defects, such as $Zr_6O_4(OH)_4$(terephthalate)$_6$ (UiO-66), approach values expected for nonporous metal particles.[52,53] The 1689 cm^{-1} solvation shell feature disappears in the *sps* polarization combination as the interfacial electric field does not align the dipoles of DMF in a parallel fashion.[54−57] A slight blue shift of the solvation shell DMF, as compared to the bulk DMF C═O mode typically occurring at 1677 cm^{-1} is due to enhancement of the solvent dielectric at a surface as compared to the bulk and is commonly observed in sum frequency experiments.[58,59] A weak feature at 1745 cm^{-1} is present in both *ssp* and *ppp* polarization schemes and can be attributed to DMF vibrational modes ordered *within* the cavity of ZIF-8; however, ongoing experiments are in progress to assign the nature of this peak.

The polarization selectivity of VSFSS allows assignment of the feature at 1774 cm^{-1}. As this vibration appears in all polarization schemes, it corresponds to C═O modes that exist in a variety of orientations relative to the interface. Additionally, the significant blue-shift of this mode, relative to the bulk DMF C═O mode, suggests a dative ligand−metal interaction. Therefore, we attribute this feature to C═O modes of DMF bound to open Zn sites (Figure 2c). DMF molecules pack around the Zn sites in directions, such as diagonal to the interface, that contain parallel and perpendicular contributions from each orientation (Figure 2b). As opposed to an ordered solvation shell, an ensemble of DMF molecules binding to Zn sites creates a feature present in all three polarization combinations. Previous reports from the MOF literature attest blue-shifting of C═O vibrational modes to when carbonyl or carboxylate groups donate lone-pair electron density to Lewis-acidic centers, such as Zn^{2+}.[60−62] While the blueshifts seen here far exceed shifts observed in bulk IR spectroscopy of C═O modes in MOFs, the interfacial environments of nanoZIF-8 vary significantly from the bulk. Interfaces, in general, present complex chemical environments, where pK_a values can shift 1−3 units more alkaline,[58] solvent dielectric constants alter by an order of magnitude,[63] sterically hindered cavities dictate reaction selectivity,[64] and molecules spontaneously undergo conformational changes.[65] Given that carbonyl modes provide sensitive probes to chemical environments for measuring changes in lipid conformation, protein structure, and ion-induced effects, it serves again here to report on the distinct chemical environments at the nanoMOF−solvent interface.[66,67]

To probe mixed solvation shells by VSFSS, we targeted perpendicular C═O modes (*ssp* polarization) of nanoZIF-8 suspended in 100% DMF, 50% DMF:50% H_2O, and 100% H_2O (Figure 2d). The 100% DMF trace shown in Figure 2d is the same as that shown in Figure 2a, with both DMF features present. When suspending nanoZIF-8 in a 50:50 mixture of DMF and water; however, the signal intensity of the lower-frequency feature (DMF solvation shell) reduces, and the higher-frequency (Zn binding) feature disappears completely. Size and zeta potential measurements were collected of these 316 nm ZIF-8 particle suspensions with mixed DMF/H_2O solvents to concurrently monitor the stability (Figure 2e). With nanoZIF-8 suspended in 100% water or DMF, zeta potentials remain large and sizes at their smallest, indicating particle stabilization. For any mixture of DMF and water (25:75, 50:50, and 75:25), however, the hydrodynamic diameters increase and zeta potentials decrease. These results suggest that competitive solvation between water and DMF increases the particle hydrodynamic radius and screens the interfacial charge. Competitive solvation has also been observed in bulk mixtures of DMF and water.[59,68] The reduction in the DMF solvation peak observed by VSFSS at 1692 cm^{-1} implies that competitive solvation with H_2O reduces the population of DMF at the interface. The disappearance of the DMF-Zn binding feature at 1774 cm^{-1} also suggests that H_2O outcompetes DMF for binding with Zn. Finally, the spectrum corresponding to 100% H_2O lacks C═O modes, as expected. Instead, the spectrum contains a small feature at 1680 cm^{-1} attributable to a water bending mode and indicative of a water solvation shell around the MOF framework.[69,70] Supplementary VSFSS experiments measuring surface DMF at ZIF-8 with the addition of electrolyte TBAPF_6 also indicate that the ordered solvent signal changes proportionally with surface charge, providing further evidence that the strength of the solvation shell and overall colloidal stability is dictated by the surface charge (Figure S7a). Due to the weakly coordinating nature of PF_6^-,[71] we expect that DMF still binds preferentially to the surface Zn^{2+} sites. Shifts in both the solvation shell and open-metal site binding features suggest that the solvation shells restructure with the addition of electrolyte. In addition to reducing the $X^{(3)}$ components in these spectra,[72] the overall reduction of integrated intensities with increasing electrolyte concentrations (Figure S7b) can be attributed to charge screening by the anions. Their presence at the slipping plane would reduce zeta potentials and, consequently, the electrostatic driving force for solvation shells to assemble.

Spontaneous Ordering within the ZIF-8 Nanoparticles. To investigate whether colloidal stability arises from excess linker binding to nanoZIF-8 open metal sites, VSFSS experiments were conducted in the C−H stretching region to detect 2-methylimidazolate ordered at the solvent−nanoparticle interface. In these experiments, deuterated DMF was used to shift the solvent C−H modes away from the frequency region of interest (2800−3000 cm^{-1}) and isolate vibrational modes arising from the linker. Figure 3a plots the resulting spectrum with a signal-to-noise ratio typically expected for crystalline materials. The data were well-fit to Voigt profile using a robust fitting routine detailed in the Supporting Information, and all peaks, including Fermi resonances, could be attributed to the expected vibrational signatures of 2-methylimidazolate (2-MIm). From the spectrum in Figure 3a, we attribute the peak at 2924 cm^{-1} to the CH_3 asymmetric stretch (plus symbol), and the feature at 2847 cm^{-1} corresponds to a CH_3 Fermi resonance (open square symbol) (Figure 3b). The high intensity peak above 3000 cm^{-1} results from a combination of both the aromatic C−H asymmetric and symmetric stretches (asterisk symbol) (Figure 3b). While we were unable to resolve a CH_3 symmetric stretch, these peak assignments are consistent with bulk IR experiments (Figure

https://doi.org/10.1021/acsnano.4c03758
ACS Nano 2024, 18, 13406−13414

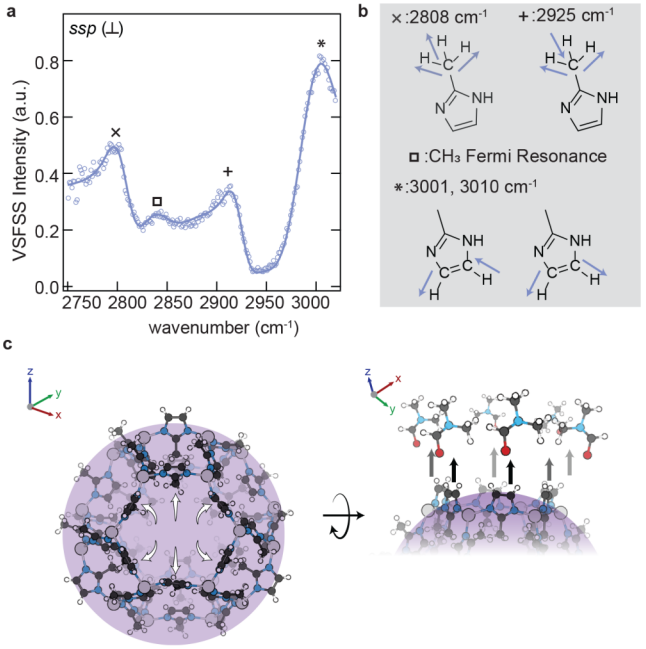

Figure 3. (a) VSFSS measurements (*ssp* polarization) of nanoZIF-8 particles suspended in d-DMF taken in the C−H stretching region. Lines represent fits of the data. (b) Illustrations of linker vibrational modes corresponding to symbols on peaks in (a). (c) Cartoon schematic demonstrating the rotational axis of 2-methylimidazole at the nanoZIF-8 interface at top-down (left) and side view (right).

S3) and recent literature[73,74] In fact, FT-IR studies into the gas sorption behavior of ZIF-8 are similarly unable to resolve the CH_3 symmetric stretch of 2-methylimidazole.[75,76] A nonresonant peak is included in the fit at 2808 cm^{-1}, which becomes most prominent in measurements of nanoZIF-8 in H_2O, a higher dielectric solvent (Figure S11). Nonresonant backgrounds are often observed in the spectra of substrates with complex or metallic compositions. As with these data, they often appear in the C−H stretching region and arise from linker-based electronic transitions that can be reduced by detiming the visible pulse in the experiment.[77−80] This approach, however, resulted in poor resolution of the resonant CH modes, prompting us to report spectra from the coherent VSFSS measurement.

Due to the noncentrosymmetric space group of ZIF-8 ($I\bar{4}3m$), we considered whether the VSFSS response in the C−H region arises from the bulk response of the linker. However, previous reports have demonstrated that introduction of solvent or other guest molecules causes the framework to adopt a centrosymmetric structure due to linker rotation.[45,81] In addition, earlier investigations have also shown that ZIF-8 in a noncentrosymmetric conformation would be VSFSS inactive because its only unique bulk nonlinear susceptibility tensor element, $X^{(2)}_{xyz}$, is null. Because the *ssp* polarization scheme used here probes the $X^{(2)}_{yyz}$ tensor element and reveals resonant vibrational modes, this intense C−H signal must arise from MOF linker spontaneously ordered at the ZIF-8 particle surface. Although we anticipated this spectrum to arise from excess ZIF-8 linker bound to the particle surface, ^{1}H NMR solution-state spectra of acid-digested particles and thermogravimetric analysis (TGA) were unable to detect excess 2-MIm (Figures S8, S9). Furthermore, if excess linker was present in quantities below the detection limit of these techniques (μmol concentrations for ^{1}H NMR and 0.1 μg masses for TGA), then such quantities are unlikely to produce the observed signal. Therefore, this SFG signal must result from the linker *within* the outermost layer of ZIF-8 nanoparticles, rather than excess linker as a capping ligand. To test whether 2-MIm binds to particle surfaces, we measured zeta potentials of ZIF-8 mixtures containing increasing quantities of additional 2-MIm, with the expectation that zeta potentials would decrease due to the presence of deprotonated imidazolate groups binding to Zn^{2+} sites. Instead, with just 25 equiv per particle, zeta potentials increased from +10 to +40 mV (Figure S10). This result suggests that 2-MIm disrupts the DMF solvation shell, which otherwise screens the positive Zn^{2+} charges from the Stern layer probed by zeta potential measurements. Instead of acting as surface capping ligands, excess 2-MIm disrupts the DMF solvation shell.[82]

The ability to detect VSFSS signal for the 2-MIm C−H vibrational modes indicates a net ordering of the linker dipoles near the solvent−nanoparticle interface, possible only if 2-MIm can rotate into a thermodynamically stable configuration (Figure 3c). Computational studies and gas adsorption experiments have reported linker rotation for ZIF-8 about its M−N bond axis.[83,84] A significant consequence of this rotational freedom is that gas molecules larger than the pore size of ZIF-8 can fit inside the framework. This phenomenon implies linker molecules could rotate and therefore "open the gate" to these larger guests species.[85] Similarly, in our work, the ability of the 2-MIm linker to rotate permits the alignment of 2-MIm vibrational dipoles at the framework interface, as shown by the VSFSS signal. VSFSS experiments probing the C−H modes on the surface of ZIF-8 were also performed in H_2O and show well-defined C−H vibrational modes attributed to the linker at similar frequencies to those seen for 2MIm in DMF (Figure S11). While ZIF-8 is hydrophobic, likely a few water molecules enter the pores and nucleate around the metal sites, as shown by theory and experiments for other MOFs with hydrophobic cores.[86,87] In both solvents studied, the rotational ability of 2-MIm promotes the filling of the solvent within the porous framework.

CONCLUSIONS

This study reports interface-specific vibrational spectra of colloidal nanoparticles and the chemical insights they enable into the nature of the solvation shells. Spectra reveal the presence of solvation shells around MOF ($Zn(2\text{-methylimidazolate})_2$) nanoparticles in aqueous, nonaqueous (DMF), and mixtures of solvent. Controlling the polarization of incident light probes the spatial arrangement of solvent molecules, while spectral shifts indicate the strength and orbital character of the solvent−nanoparticle interactions. Differences between the spectra of these materials, therefore, uncover the microscopic details of material-specific solvation shells. Unexpectedly, VSFSS also revealed the vibrational signatures of the nanoparticle, in addition to solvent, providing direct evidence of spontaneous order of nanometers of molecular dipoles on either side of the nanoparticle−solvent interface. These results lay the groundwork for applying VSFSS as one of the surface-specific techniques for understanding the interfacial chemistry of colloidal nanoparticles.

https://doi.org/10.1021/acsnano.4c03758
ACS Nano 2024, 18, 13406−13414

METHODS

Vibrational Sum Frequency Scattering Spectroscopy. Vibrational sum frequency scattering spectroscopy (VSFSS) is a second-order nonlinear spectroscopic technique that provides molecular-level information at buried curved surfaces and is similar to the technique of reflection vibrational sum frequency generation at planar interfaces.[21,88] Specifically, VSFSS is capable of probing colloidal interfaces such as those of nanoparticles, nanoemulsions, and the nanometal organic frameworks used in this study.[43,46,89−91] Due to symmetry considerations, sum frequency generation is forbidden in bulk media and a sum frequency response can be measured only in a noncentrosymmetric environment. In this case, at the nanoMOF/solvent interface, the inversion symmetry is broken, thus allowing interfacial resonances to be investigated. The coherence length of the sample is significantly larger than the size of the nanoparticle, thus resulting in quasi-phase matching.[90] More detailed and rigorous theory describing sum frequency generation and sum frequency scattering can be found elsewhere.[22,30]

The VSFSS experimental setup used for this work has been described in previous publications.[92,93] Here, we provide a brief summary and a representative schematic (Figure S4). A Ti:sapphire regenerative amplifier laser (Coherent Libra) was used to generate an 800 nm, ∼80 fs fundamental beam with a 1 kHz repetition rate. The fundamental beam is split such that one portion is used as the visible beam, while the remaining portion is sent through an optical parametric amplifier (Coherent OPerA Solo) to generate a variable broadband infrared (IR) beam through difference frequency generation. For the experiments described here, the IR wavelength was set to probe either the C═O or C−H vibrational resonance. The visible and IR beams are then sent through a series of mirrors, lenses, and polarizers, until they are spatially and temporally overlapped in the sample cuvette containing the MOF sample. The sample cell was composed of a CaF_2 entrance window and a quartz cuvette backing (Helma QS) with an optical path length of 200 μm. The IR beam was focused down with a 90° parabolic gold mirror (focal length of ∼50 mm) to obtain a spot size of ∼80 μm. The visible beam focus after the sample cell results in a spot size of ∼500 μm in the sample. The visible and IR light interact with the sample and generate a scattered SF response, which is collected at an angle of ∼60° (with respect to the forward direction), collimated with a plano-convex lens (focal length ∼20 mm), focused (focal length ∼100 mm) into a spectrometer (Princeton Instruments IsoPlane SCT320), and then spectrally dispersed on an intensified CCD (Princeton Instruments PI-MAX4).

Each VSFSS sample consists of 80 μL of a freshly sonicated nanoparticle suspension prepared at a concentration of 5 mg/mL. The ZIF-8 particles measured here exhibit crystallite domain sizes of 96 nm as determined by Scherrer analysis (Figure S2). By SEM, particle sizes average to 316 nm. When suspended in DMF, H_2O, or solvent mixtures, all samples exhibit slight swelling to hydrodynamic diameters of ∼300−400 nm. This increase in the hydrodynamic diameter arises from the presence of self-assembled solvation shells with finite diameters in solution. Because the DLS sizes appear only slightly larger than the SEM sizes, we conclude that size contributions from particle aggregation are minor. Extended details regarding the normalization of the sum frequency scattered responses as a function of particle diameter are described in the Supporting Information.

The polarization of the visible, IR, and sum frequency beams can be selected to probe specific dipole components of the vibrational modes. Spectra collected in the C═O stretching region used either the *ssp*, *ppp*, or *sps* polarization combination, with each letter denoting the polarization of the sum frequency, visible, and IR beams, respectively. In the C−H stretching region, spectra were collected in the *ssp* polarization. Under the current experimental setup, *ssp* probes molecular dipole components of the transition dipole moments perpendicular to the to the particle surface, while *sps* probes components of the transition moments parallel to the particle surface. *ppp* probes all of the oriented molecular dipoles. For all experiments, the incident visible pulse energy was 25 μJ, while the IR pulse energies were 2−4 μJ and 5 μJ for the C═O and C−H stretching regions, respectively.

All spectra are worked up in Igor Pro and follow a rigorous normalization and fitting routine. A single trace in a final figure is the result of 3−5 averaged trials with each trial consisting of 2 signal measurements and 2 background measurements. Each trial is averaged, background subtracted, and normalized by a nonresonant response from $KNbO_3$ to account for IR pulse shape. In the C−H region, trials are also normalized through dividing by the integrated intensity between 2800 and 3000 cm^{-1} generated from a reference *d*-hexadecane in D_2O nanoemulsion stabilized with 1 mM AOT (a commonly used surfactant and explored thoroughly in other work from the Richmond laboratory).[92] Finally, every trial is normalized by the size of the nanoparticle through a scattering routine developed by Roke et al. that simulates the percentage of scattered signal captured from a measurement of 60°, which is dependent on particle size and polarization schemes.[94,95]

In VSFSS, the intensity of the scattered SF response is proportional to the intensities of the incoming visible and IR beams ($I_{IR}I_{vis}$) and the square modulus of the second-order nonlinear susceptibility ($X^{(2)}$):

$$I_{VSFS} \propto X^{(2)} I_{IR} I_{vis}$$

The $X^{(2)}$ has nonresonant and resonant terms, which are accounted for in the fitting equation here as developed by Bain et al.[96]

$$|X(\omega)^{(2)}|^2 = |X_{NR}^{(2)} e^{i\phi} + \sum_v \int_{-\infty}^{+\infty} \frac{A_v e^{i\phi_v} e^{-\left(\frac{\omega_L-\omega_v}{\Gamma_v}\right)^2}}{\omega_L - \omega_{IR} + i\Gamma_L} d\omega_L|^2$$

where the amplitude of the nonresonant susceptibility is described by $X_{NR}^{(2)}$ with a phase ϕ. The summation of all vibrational transitions that are SF active describes the resonant susceptibility, where A_v is the peak amplitude, ϕ is the phase, Γ_L is the Lorentzian line width describing homogeneous broadening, and Γ_v is the Gaussian line width describing inhomogeneous broadening. The Richmond/Scatena lab fitting routine uses eq 2 in an algorithm developed by Fred G. Moore to fit all experimental spectra.

All spectra collected in the C═O stretching region are fit to a background feature that accounts for the elevated baseline. Experimentally, this background is due to a nonresonant electrical response and is reduced by detiming the overlap between the visible and IR beams.[46,72,97] Tables S1−S4 list the fitting parameters used to fit all of the VSFSS data in this work.

ASSOCIATED CONTENT

Supporting Information

The Supporting Information is available free of charge at https://pubs.acs.org/doi/10.1021/acsnano.4c03758.

Materials, synthetic procedures, nanoparticle characterization (Figure S1−S3, S6, S8−S10), description of techniques (Figure S4), VSFSS solvation absorption spectra (Figure S5), VSFSS spectra with electrolyte (Figure S7), VSFSS linker spectra (Figure S11), and fitting parameters (Tables S1−S4) (PDF)

AUTHOR INFORMATION

Corresponding Author

Carl K. Brozek − *Department of Chemistry and Biochemistry, Materials Science Institute, University of Oregon, Eugene, Oregon 97403, United States;* orcid.org/0000-0002-8014-7904; Email: cbrozek@uoregon.edu

Authors

Ashley N. Mapile − *Department of Chemistry and Biochemistry, Materials Science Institute, University of*

https://doi.org/10.1021/acsnano.4c03758
ACS Nano 2024, 18, 13406−13414

Oregon, Eugene, Oregon 97403, United States; orcid.org/0000-0002-7808-4692

Michael A. LeRoy − *Department of Chemistry and Biochemistry, Materials Science Institute, University of Oregon, Eugene, Oregon 97403, United States;* orcid.org/0000-0002-7715-7685

Kevin Fabrizio − *Department of Chemistry and Biochemistry, Materials Science Institute, University of Oregon, Eugene, Oregon 97403, United States;* orcid.org/0000-0001-9700-1824

Lawrence F. Scatena − *Department of Chemistry and Biochemistry, Materials Science Institute, University of Oregon, Eugene, Oregon 97403, United States;* orcid.org/0000-0003-2466-8825

Complete contact information is available at: https://pubs.acs.org/10.1021/acsnano.4c03758

Author Contributions

The manuscript was written through contributions of all authors. All authors have given approval to the final version of the manuscript.

Funding

This work made use of the CAMCOR facility of the Lorry I. Lokey Laboratories at the University of Oregon to perform SEM experiments. This material is based upon work supported by the National Science Foundation through the Division of Materials Research under grant no. DMR-2114430 and the Division of Chemistry under grant no. CHE-2003526. C.K.B. acknowledges the Research Corporation for Science Advancement (Cottrell Award).

Notes

The authors declare no competing financial interest.

ACKNOWLEDGMENTS

We thank D. C. Johnson, M. C. Lonergan, F. G. Moore, and S. Boettcher for advice, discussion, and review of the manuscript. We thank E. Tran for assistance at the conception of this project. We thank G. L. Richmond for foundational work and inspiration.

REFERENCES

(1) Schirò, G.; Fichou, Y.; Gallat, F.-X.; Wood, K.; Gabel, F.; Moulin, M.; Härtlein, M.; Heyden, M.; Colletier, J.-P.; Orecchini, A.; et al. Translational Diffusion of Hydration Water Correlates with Functional Motions in Folded and Intrinsically Disordered Proteins. *Nat. Commun.* **2015**, *6* (1), 6490.

(2) Bellissent-Funel, M.-C.; Hassanali, A.; Havenith, M.; Henchman, R.; Pohl, P.; Sterpone, F.; van der Spoel, D.; Xu, Y.; Garcia, A. E. Water Determines the Structure and Dynamics of Proteins. *Chem. Rev.* **2016**, *116* (13), 7673−7697.

(3) Zobel, M.; Neder, R. B.; Kimber, S. A. J. Universal Solvent Restructuring Induced by Colloidal Nanoparticles. *Science* **2015**, *347* (6219), 292−294.

(4) Larson, R. G.; Kotov, N. A. Nonadditivity of Nanoparticle Interactions. *Science* **2015**, *350* (6257), 1242477.

(5) Thomä, S. L. J.; Krauss, S. W.; Eckardt, M.; Chater, P.; Zobel, M. Atomic Insight into Hydration Shells around Facetted Nanoparticles. *Nat. Commun.* **2019**, *10* (1), 995.

(6) Derjaguin, B. V.; Churaev, N. V.; Muller, V. M. The Derjaguin−Landau−Verwey−Overbeek (DLVO) Theory of Stability of Lyophobic Colloids. In *Surface Forces*; Derjaguin, B. V.; Churaev, N. V.; Muller, V. M., Eds.; Springer: Boston, MA, 1987; pp. 293−310. DOI: .

(7) Calvin, J. J.; Brewer, A. S.; Alivisatos, A. P. The Role of Organic Ligand Shell Structures in Colloidal Nanocrystal Synthesis. *Nat. Synth.* **2022**, *1* (2), 127−137.

(8) Israelachvili, J.; Wennerström, H. Role of Hydration and Water Structure in Biological and Colloidal Interactions. *Nature* **1996**, *379* (6562), 219−225.

(9) Li, Z.; Ruiz, V. G.; Kanduč, M.; Dzubiella, J. Ion-Specific Adsorption on Bare Gold (Au) Nanoparticles in Aqueous Solutions: Double-Layer Structure and Surface Potentials. *Langmuir* **2020**, *36* (45), 13457−13468.

(10) Petersen, N.; Girard, M.; Riedinger, A.; Valsson, O. The Crucial Role of Solvation Forces in the Steric Stabilization of Nanoplatelets. *Nano Lett.* **2022**, *22* (24), 9847−9853.

(11) Israelachvili, J. N.; McGuiggan, P. M. Forces Between Surfaces in Liquids. *Science* **1988**, *241* (4867), 795−800.

(12) Valtiner, M.; Banquy, X.; Kristiansen, K.; Greene, G. W.; Israelachvili, J. N. The Electrochemical Surface Forces Apparatus: The Effect of Surface Roughness, Electrostatic Surface Potentials, and Anodic Oxide Growth on Interaction Forces, and Friction between Dissimilar Surfaces in Aqueous Solutions. *Langmuir* **2012**, *28* (36), 13080−13093.

(13) Bischoff, M.; Biriukov, D.; Předota, M.; Marchioro, A. Second Harmonic Scattering Reveals Ion-Specific Effects at the SiO_2 and TiO_2 Nanoparticle/Aqueous Interface. *J. Phys. Chem. C* **2021**, *125* (45), 25261−25274.

(14) Bischoff, M.; Kim, N. Y.; Joo, J. B.; Marchioro, A. Water Orientation at the Anatase TiO_2 Nanoparticle Interface: A Probe of Surface pKa Values. *J. Phys. Chem. Lett.* **2022**, *13*, 8677−8683.

(15) Yakin, F. E.; Barisik, M.; Sen, T. Pore Size and Porosity Dependent Zeta Potentials of Mesoporous Silica Nanoparticles. *J. Phys. Chem. C* **2020**, *124* (36), 19579−19587.

(16) Murota, K.; Saito, T. Pore Size Effects on Surface Charges and Interfacial Electrostatics of Mesoporous Silicas. *Phys. Chem. Chem. Phys.* **2022**, *24* (30), 18073−18082.

(17) Sen, T.; Barisik, M. Internal Surface Electric Charge Characterization of Mesoporous Silica. *Sci. Rep.* **2019**, *9* (1), 137.

(18) Salis, A.; Parsons, D. F.; Boström, M.; Medda, L.; Barse, B.; Ninham, B. W.; Monduzzi, M. Ion Specific Surface Charge Density of SBA-15 Mesoporous Silica. *Langmuir* **2010**, *26* (4), 2484−2490.

(19) Abendroth, R. P. Surface Charge Development of Porous Silica in Aqueous Solution. *J. Phys. Chem.* **1972**, *76* (18), 2547−2549.

(20) Chen, C.-Y.; Hsieh, M.-J.; Raj, A.; Peng, W.-C.; Hamaguchi, H.; Chuang, W.-T.; Wang, X.; Wang, C.-L. Missing Piece in Colloidal Stability−Morphological Factor of Hydrophobic Nanoparticles. *Langmuir* **2023**, *39* (8), 2922−2931.

(21) Roke, S.; Roeterdink, W. G.; Wijnhoven, J. E. G. J.; Petukhov, A. V.; Kleyn, A. W.; Bonn, M. Vibrational Sum Frequency Scattering from a Submicron Suspension. *Phys. Rev. Lett.* **2003**, *91* (25), 258302.

(22) Shen, Y. R. Surface Properties Probed by Second-Harmonic and Sum-Frequency Generation. *Nature* **1989**, *337* (6207), 519−525.

(23) Gragson, D. E.; Richmond, G. L. Comparisons of the Structure of Water at Neat Oil/Water and Air/Water Interfaces As Determined by Vibrational Sum Frequency Generation. *Langmuir* **1997**, *13* (18), 4804−4806.

(24) Scatena, L. F.; Brown, M. G.; Richmond, G. L. Water at Hydrophobic Surfaces: Weak Hydrogen Bonding and Strong Orientation Effects. *Science* **2001**, *292* (5518), 908−912.

(25) Wang, H.; Xu, Q.; Liu, Z.; Tang, Y.; Wei, G.; Shen, Y. R.; Liu, W.-T. Gate-Controlled Sum-Frequency Vibrational Spectroscopy for Probing Charged Oxide/Water Interfaces. *J. Phys. Chem. Lett.* **2019**, *10* (19), 5943−5948.

(26) Rehl, B.; Ma, E.; Parshotam, S.; DeWalt-Kerian, E. L.; Liu, T.; Geiger, F. M.; Gibbs, J. M. Water Structure in the Electrical Double Layer and the Contributions to the Total Interfacial Potential at Different Surface Charge Densities. *J. Am. Chem. Soc.* **2022**, *144* (36), 16338−16349.

(27) Carpenter, A. P.; Tran, E.; Altman, R. M.; Richmond, G. L. Formation and Surface-Stabilizing Contributions to Bare Nano-

emulsions Created with Negligible Surface Charge. *Proc. Natl. Acad. Sci. U. S. A.* **2019**, *116* (19), 9214−9219.
(28) Pullanchery, S.; Kulik, S.; Rehl, B.; Hassanali, A.; Roke, S. Charge Transfer across C−H···O Hydrogen Bonds Stabilizes Oil Droplets in Water. *Science* **2021**, *374* (6573), 1366−1370.
(29) Wang, H.-F.; Velarde, L.; Gan, W.; Fu, L. Quantitative Sum-Frequency Generation Vibrational Spectroscopy of Molecular Surfaces and Interfaces: Lineshape, Polarization, and Orientation. *Annu. Rev. Phys. Chem.* **2015**, *66* (1), 189−216.
(30) Lambert, A. G.; Davies, P. B.; Neivandt, D. J. Implementing the Theory of Sum Frequency Generation Vibrational Spectroscopy: A Tutorial Review. *Appl. Spectrosc. Rev.* **2005**, *40* (2), 103−145.
(31) Farha, O. K.; Eryazici, I.; Jeong, N. C.; Hauser, B. G.; Wilmer, C. E.; Sarjeant, A. A.; Snurr, R. Q.; Nguyen, S. T.; Yazaydın, A. Ö.; Hupp, J. T. Metal−Organic Framework Materials with Ultrahigh Surface Areas: Is the Sky the Limit? *J. Am. Chem. Soc.* **2012**, *134* (36), 15016−15021.
(32) Marshall, C. R.; Timmel, E. E.; Staudhammer, S. A.; Brozek, C. K. Experimental Evidence for a General Model of Modulated MOF Nanoparticle Growth. *Chem. Sci.* **2020**, *11* (42), 11539−11547.
(33) Marshall, C. R.; Staudhammer, S. A.; Brozek, C. K. Size Control over Metal−Organic Framework Porous Nanocrystals. *Chem. Sci.* **2019**, *10* (41), 9396−9408.
(34) Marshall, C. R.; Dvorak, J. P.; Twight, L. P.; Chen, L.; Kadota, K.; Andreeva, A. B.; Overland, A. E.; Ericson, T.; Cozzolino, A. F.; Brozek, C. K. Size-Dependent Properties of Solution-Processable Conductive MOF Nanocrystals. *J. Am. Chem. Soc.* **2022**, *144* (13), 5784−5794.
(35) Troyano, J.; Carné-Sánchez, A.; Avci, C.; Imaz, I.; Maspoch, D. Colloidal Metal−Organic Framework Particles: The Pioneering Case of ZIF-8. *Chem. Soc. Rev.* **2019**, *48* (23), 5534−5546.
(36) Fonseca, J.; Meng, L.; Imaz, I.; Maspoch, D. Self-Assembly of Colloidal Metal−Organic Framework (MOF) Particles. *Chem. Soc. Rev.* **2023**, *52* (7), 2528−2543.
(37) Rojas, S.; Carmona, F. J.; Maldonado, C. R.; Horcajada, P.; Hidalgo, T.; Serre, C.; Navarro, J. A. R.; Barea, E. Nanoscaled Zinc Pyrazolate Metal−Organic Frameworks as Drug-Delivery Systems. *Inorg. Chem.* **2016**, *55* (5), 2650−2663.
(38) Carey, C. A.; Devlin, A. M.; Matzger, A. J. Dual Modification of MOFs Improves Dispersion and Ionic Conductivity of Mixed Matrix Membranes. *ACS Mater. Lett.* **2024**, *6*, 159−164.
(39) Yadav, P.; Kumari, S.; Yadav, A.; Bhardwaj, P.; Maruthi, M.; Chakraborty, A.; Kanoo, P. Biocompatible Drug Delivery System Based on a MOF Platform for a Sustained and Controlled Release of the Poorly Soluble Drug Norfloxacin. *ACS Omega* **2023**, *8* (31), 28367−28375.
(40) Tong, P.; Zhu, L.; Zang, Y.; Li, J.; He, X.; James, T. D. Metal−organic frameworks (MOFs) as host materials for the enhanced delivery of biomacromolecular therapeutics. *Chem. Commun.* **2021**, *57* (91), 12098−12110.
(41) Lin, R.; Villacorta Hernandez, B.; Ge, L.; Zhu, Z. Metal Organic Framework Based Mixed Matrix Membranes: An Overview on Filler/Polymer Interfaces. *J. Mater. Chem. A* **2018**, *6* (2), 293−312.
(42) Datta, S. J.; Mayoral, A.; Murthy Srivatsa Bettahalli, N.; Bhatt, P. M.; Karunakaran, M.; Carja, I. D.; Fan, D.; Graziane, M.; Mileo, P.; Semino, R.; et al. Rational Design of Mixed-Matrix Metal-Organic Framework Membranes for Molecular Separations. *Science* **2022**, *376* (6597), 1080−1087.
(43) Bordenyuk, A. N.; Weeraman, C.; Yatawara, A.; Jayathilake, H. D.; Stiopkin, I.; Liu, Y.; Benderskii, A. V. Vibrational Sum Frequency Generation Spectroscopy of Dodecanethiol on Metal Nanoparticles. *J. Phys. Chem. C* **2007**, *111* (25), 8925−8933.
(44) Watson, B. R.; Ma, Y.-Z.; Cahill, J. F.; Doughty, B.; Calhoun, T. R. Probing Ligand Removal and Ordering at Quantum Dot Surfaces Using Vibrational Sum Frequency Generation Spectroscopy. *J. Colloid Interface Sci.* **2019**, *537*, 389−395.
(45) Wagner, J. C.; Hunter, K. M.; Paesani, F.; Xiong, W. Water Capture Mechanisms at Zeolitic Imidazolate Framework Interfaces. *J. Am. Chem. Soc.* **2021**, *143* (50), 21189−21194.
(46) Foster, M. J.; Carpenter, A. P.; Richmond, G. L. Dynamic Duo: Vibrational Sum Frequency Scattering Investigation of pH-Switchable Carboxylic Acid/Carboxylate Surfactants on Nanodroplet Surfaces. *J. Phys. Chem. B* **2021**, *125* (33), 9629−9640.
(47) Tran, E.; Richmond, G. L. Interfacial Steric and Molecular Bonding Effects Contributing to the Stability of Neutrally Charged Nanoemulsions. *Langmuir* **2021**, *37* (43), 12643−12653.
(48) Shen, Y. R.; Ostroverkhov, V. Sum-Frequency Vibrational Spectroscopy on Water Interfaces: Polar Orientation of Water Molecules at Interfaces. *Chem. Rev.* **2006**, *106* (4), 1140−1154.
(49) Zhang, C.; Han, C.; Sholl, D. S.; Schmidt, J. R. Computational Characterization of Defects in Metal−Organic Frameworks: Spontaneous and Water-Induced Point Defects in ZIF-8. *J. Phys. Chem. Lett.* **2016**, *7* (3), 459−464.
(50) Möslein, A. F.; Donà, L.; Civalleri, B.; Tan, J.-C. Defect Engineering in Metal−Organic Framework Nanocrystals: Implications for Mechanical Properties and Performance. *ACS Appl. Nano Mater.* **2022**, *5* (5), 6398−6409.
(51) Oh, S.; Lee, S.; Lee, G.; Oh, M. Enhanced Adsorption Capacity of ZIF-8 for Chemical Warfare Agent Simulants Caused by Its Morphology and Surface Charge. *Sci. Rep.* **2023**, *13* (1), 12250.
(52) Morris, W.; Wang, S.; Cho, D.; Auyeung, E.; Li, P.; Farha, O. K.; Mirkin, C. A. Role of Modulators in Controlling the Colloidal Stability and Polydispersity of the UiO-66 Metal−Organic Framework. *ACS Appl. Mater. Interfaces* **2017**, *9* (39), 33413−33418.
(53) Ibrahim, A. H.; El-Mehalmey, W. A.; Haikal, R. R.; Safy, M. E. A.; Amin, M.; Shatla, H. R.; Karakalos, S. G.; Alkordi, M. H. Tuning the Chemical Environment within the UiO-66-NH_2 Nanocages for Charge-Dependent Contaminant Uptake and Selectivity. *Inorg. Chem.* **2019**, *58* (22), 15078−15087.
(54) Shin, S.-J.; Gittins, J. W.; Golomb, M. J.; Forse, A. C.; Walsh, A. Microscopic Origin of Electrochemical Capacitance in Metal−Organic Frameworks. *J. Am. Chem. Soc.* **2023**, *145* (26), 14529−14538.
(55) Lian, C.; Jiang, D.; Liu, H.; Wu, J. A Generic Model for Electric Double Layers in Porous Electrodes. *J. Phys. Chem. C* **2016**, *120* (16), 8704−8710.
(56) Costentin, C.; Savéant, J.-M. Electrochemical Capacitive Charging in Porous Materials. Discriminating between Ohmic Potential Drop and Counterion Diffusion. *ACS Appl. Energy Mater.* **2019**, *2* (7), 4981−4986.
(57) Biesheuvel, P. M.; Fu, Y.; Bazant, M. Z. Diffuse Charge and Faradaic Reactions in Porous Electrodes. *Phys. Rev. E* **2011**, *83* (6), 061507.
(58) Andino, R. S.; Liu, J.; Miller, C. M.; Chen, X.; Devlin, S. W.; Hong, M. K.; Rajagopal, R.; Erramilli, S.; Ziegler, L. D. Anomalous pH-Dependent Enhancement of p-Methyl Benzoic Acid Sum-Frequency Intensities: Cooperative Surface Adsorption Effects. *J. Phys. Chem. A* **2020**, *124* (16), 3064−3076.
(59) Koverga, V.; Juhász, Á.; Dudariev, D.; Lebedev, M.; Idrissi, A.; Jedlovszky, P. Local Structure of DMF−Water Mixtures, as Seen from Computer Simulations and Voronoi Analysis. *J. Phys. Chem. B* **2022**, *126*, 6964.
(60) Koch, D.; Chen, Y.; Golub, P.; Manzhos, S. Revisiting π Backbonding: The Influence of d Orbitals on Metal−CO Bonds and Ligand Red Shifts. *Phys. Chem. Chem. Phys.* **2019**, *21* (37), 20814−20821.
(61) Kawasaki, H.; Yamamoto, H.; Fujimori, H.; Arakawa, R.; Iwasaki, Y.; Inada, M. Stability of the DMF-Protected Au Nanoclusters: Photochemical, Dispersion, and Thermal Properties. *Langmuir* **2010**, *26* (8), 5926−5933.
(62) Mittal, A.; Gandhi, S.; Roy, I. Mechanistic Interaction Studies of Synthesized ZIF-8 Nanoparticles with Bovine Serum Albumin Using Spectroscopic and Molecular Docking Approaches. *Sci. Rep.* **2022**, *12* (1), 10331.
(63) Sorenson, S. A.; Patrow, J. G.; Dawlaty, J. M. Solvation Reaction Field at the Interface Measured by Vibrational Sum Frequency Generation Spectroscopy. *J. Am. Chem. Soc.* **2017**, *139* (6), 2369−2378.

https://doi.org/10.1021/acsnano.4c03758
ACS Nano 2024, 18, 13406−13414

(64) Yin, F.; Hu, P.; Ma, Y.-H.; Luo, Y.; Wang, C.; Zhu, W.; Lu, X. Polar Solvents Induce Sum Frequency Generation Activity for Multiwalled Carbon Nanotubes. *Langmuir* **2021**, *37* (21), 6540−6548.
(65) Wang, Z.; Lin, H.; Zhang, X.; Li, J.; Chen, X.; Wang, S.; Gong, W.; Yan, H.; Zhao, Q.; Lv, W.; et al. Revealing Molecular Conformation−Induced Stress at Embedded Interfaces of Organic Optoelectronic Devices by Sum Frequency Generation Spectroscopy. *Sci. Adv.* **2021**, *7* (16), No. eabf8555.
(66) Dreier, L. B.; Bonn, M.; Backus, E. H. G. Hydration and Orientation of Carbonyl Groups in Oppositely Charged Lipid Monolayers on Water. *J. Phys. Chem. B* **2019**, *123* (5), 1085−1089.
(67) Li, X.; Roiaz, M.; Pramhaas, V.; Rameshan, C.; Rupprechter, G. Polarization-Dependent SFG Spectroscopy of Near Ambient Pressure CO Adsorption on Pt(111) and Pd(111) Revisited. *Top. Catal.* **2018**, *61* (9−11), 751−762.
(68) Tomar, D.; Rana, B.; Jena, K. C. The Structure of Water−DMF Binary Mixtures Probed by Linear and Nonlinear Vibrational Spectroscopy. *J. Chem. Phys.* **2020**, *152* (11), 114707.
(69) Vinaykin, M.; Benderskii, A. V. Vibrational Sum-Frequency Spectrum of the Water Bend at the Air/Water Interface. *J. Phys. Chem. Lett* **2012**, *3* (22), 3348−3352.
(70) Seki, T.; Yu, C.-C.; Chiang, K.-Y.; Tan, J.; Sun, S.; Ye, S.; Bonn, M.; Nagata, Y. Disentangling Sum-Frequency Generation Spectra of the Water Bending Mode at Charged Aqueous Interfaces. *J. Phys. Chem. B* **2021**, *125* (25), 7060−7067.
(71) Honeychuck, R. V.; Hersh, W. H. Coordination of "Non-coordinating" Anions: Synthesis, Characterization, and x-Ray Crystal Structures of Fluorine-Bridged Hexafluoroantimonate(1-), Tetrafluoroborate(1-), and Hexafluorophosphate(1-) Adducts of $[R3P(CO)_3(NO)W]^+$. An Unconventional Order of Anion Donor Strength. *Inorg. Chem.* **1989**, *28* (14), 2869−2886.
(72) Ohno, P. E.; Wang, H.; Geiger, F. M. Second-Order Spectral Lineshapes from Charged Interfaces. *Nat. Commun.* **2017**, *8* (1), 1032.
(73) Di Santo, A.; Pérez, H.; Echeverría, G. A.; Piro, O. E.; Iglesias, R. A.; Carbonio, R. E.; Ben Altabef, A.; Gil, D. M. Exploring Weak Intermolecular Interactions in Thiocyanate-Bonded Zn(II) and Cd(II) Complexes with Methylimidazole: Crystal Structures, Hirshfeld Surface Analysis and Luminescence Properties. *RSC Adv.* **2018**, *8* (42), 23891−23902.
(74) Zhang, Y.; Jia, Y.; Li, M.; Hou, L. Influence of the 2-Methylimidazole/Zinc Nitrate Hexahydrate Molar Ratio on the Synthesis of Zeolitic Imidazolate Framework-8 Crystals at Room Temperature. *Sci. Rep.* **2018**, *8* (1), 9597.
(75) Hu, Y.; Kazemian, H.; Rohani, S.; Huang, Y.; Song, Y. In Situ High Pressure Study of ZIF-8 by FTIR Spectroscopy. *Chem. Commun.* **2011**, *47* (47), 12694.
(76) Hu, Y.; Liu, Z.; Xu, J.; Huang, Y.; Song, Y. Evidence of Pressure Enhanced CO_2 Storage in ZIF-8 Probed by FTIR Spectroscopy. *J. Am. Chem. Soc.* **2013**, *135* (25), 9287−9290.
(77) Curtis, A. D.; Reynolds, S. B.; Calchera, A. R.; Patterson, J. E. Understanding the Role of Nonresonant Sum-Frequency Generation from Polystyrene Thin Films. *J. Phys. Chem. Lett.* **2010**, *1* (16), 2435−2439.
(78) Backus, E. H. G.; Garcia-Araez, N.; Bonn, M.; Bakker, H. J. On the Role of Fresnel Factors in Sum-Frequency Generation Spectroscopy of Metal−Water and Metal-Oxide−Water Interfaces. *J. Phys. Chem. C* **2012**, *116* (44), 23351−23361.
(79) Wallentine, S.; Bandaranayake, S.; Biswas, S.; Baker, L. R. Plasmon-Resonant Vibrational Sum Frequency Generation of Electrochemical Interfaces: Direct Observation of Carbon Dioxide Electroreduction on Gold. *J. Phys. Chem. A* **2020**, *124* (39), 8057−8064.
(80) Li, B.; Ma, Y.; Han, X.; Hu, P.; Lu, X. Enhanced Sum Frequency Generation for Monolayers on Au Relative to Silica: Local Field Factors and SPR Effect. *Langmuir* **2023**, *39* (1), 659−667.
(81) Van Cleuvenbergen, S.; Stassen, I.; Gobechiya, E.; Zhang, Y.; Markey, K.; De Vos, D. E.; Kirschhock, C.; Champagne, B.; Verbiest, T.; van der Veen, M. A. ZIF-8 as Nonlinear Optical Material: Influence of Structure and Synthesis. *Chem. Mater.* **2016**, *28* (9), 3203−3209.
(82) Van Cleuvenbergen, S.; Smith, Z. J.; Deschaume, O.; Bartic, C.; Wachsmann-Hogiu, S.; Verbiest, T. Morphology and Structure of ZIF-8 during Crystallisation Measured by Dynamic Angle-Resolved Second Harmonic Scattering. *Nat. Commun.* **2018**, *9* (1), 3418.
(83) Zhou, W.; Wu, H.; Udovic, T. J.; Rush, J. J.; Yildirim, T. Quasi-Free Methyl Rotation in Zeolitic Imidazolate Framework-8. *J. Phys. Chem. A* **2008**, *112* (49), 12602−12606.
(84) Kolokolov, D. I.; Stepanov, A. G.; Jobic, H. Mobility of the 2-Methylimidazolate Linkers in ZIF-8 Probed by 2H NMR: Saloon Doors for the Guests. *J. Phys. Chem. C* **2015**, *119* (49), 27512−27520.
(85) Fairen-Jimenez, D.; Moggach, S. A.; Wharmby, M. T.; Wright, P. A.; Parsons, S.; Düren, T. Opening the Gate: Framework Flexibility in ZIF-8 Explored by Experiments and Simulations. *J. Am. Chem. Soc.* **2011**, *133* (23), 8900−8902.
(86) Rieth, A. J.; Hunter, K. M.; Dincă, M.; Paesani, F. Hydrogen Bonding Structure of Confined Water Templated by a Metal-Organic Framework with Open Metal Sites. *Nat. Commun.* **2019**, *10* (1), 4771.
(87) Valentine, M. L.; Yin, G.; Oppenheim, J. J.; Dincă, M.; Xiong, W. Ultrafast Water H-Bond Rearrangement in a Metal−Organic Framework Probed by Femtosecond Time-Resolved Infrared Spectroscopy. *J. Am. Chem. Soc.* **2023**, *145* (21), 11482−11487.
(88) Moore, F. G.; Richmond, G. L. Integration or Segregation: How Do Molecules Behave at Oil/Water Interfaces? *Acc. Chem. Res.* **2008**, *41* (6), 739−748.
(89) Makarem, M.; Lee, C. M.; Sawada, D.; O'Neill, H. M.; Kim, S. H. Distinguishing Surface versus Bulk Hydroxyl Groups of Cellulose Nanocrystals Using Vibrational Sum Frequency Generation Spectroscopy. *J. Phys. Chem. Lett.* **2018**, *9* (1), 70−75.
(90) Roke, S.; Gonella, G. Nonlinear Light Scattering and Spectroscopy of Particles and Droplets in Liquids. *Annu. Rev. Phys. Chem.* **2012**, *63* (1), 353−378.
(91) Tran, E.; Mapile, A. N.; Richmond, G. L. Peeling Back the Layers: Investigating the Effects of Polyelectrolyte Layering on Surface Structure and Stability of Oil-in-Water Nanoemulsions. *J. Colloid Interface Sci.* **2021**, *599*, 706−716.
(92) Hensel, J. K.; Carpenter, A. P.; Ciszewski, R. K.; Schabes, B. K.; Kittredge, C. T.; Moore, F. G.; Richmond, G. L. Molecular Characterization of Water and Surfactant AOT at Nanoemulsion Surfaces. *Proc. Natl. Acad. Sci. U. S. A.* **2017**, *114* (51), 13351−13356.
(93) Tran, E.; Carpenter, A. P.; Richmond, G. L. Probing the Molecular Structure of Coadsorbed Polyethylenimine and Charged Surfactants at the Nanoemulsion Droplet Surface. *Langmuir* **2020**, *36* (31), 9081−9089.
(94) *NLS-Simulate 1.0*. Software Informer. https://nls-simulate.software.informer.com/. (accessed 2022−06−06).
(95) de Beer, A. G. F.; Roke, S.; Dadap, J. I. Theory of Optical Second-Harmonic and Sum-Frequency Scattering from Arbitrarily Shaped Particles. *J. Opt. Soc. Am. B* **2011**, *28* (6), 1374−1384.
(96) Bain, C. D.; Davies, P. B.; Ong, T. H.; Ward, R. N.; Brown, M. A. Quantitative Analysis of Monolayer Composition by Sum-Frequency Vibrational Spectroscopy. *Langmuir* **1991**, *7* (8), 1563−1566.
(97) Schmüser, L.; Golbek, T. W.; Weidner, T. Windowless Detection Geometry for Sum Frequency Scattering Spectroscopy in the C-D and Amide I Regions. *Biointerphases* **2021**, *16* (1), 011201.

https://doi.org/10.1021/acsnano.4c03758
ACS Nano 2024, 18, 13406−13414